

Rotation of Two Micron All Sky Survey Clumps in Molecular Clouds

XUEFANG XU ^(),^{1,2} DI LI ^(),^{1,2,3} Y.SOPHIA DAI ^(),⁴ PAUL F. GOLDSMITH,⁵ AND GARY A. FULLER⁶

¹*CAS Key Laboratory of FAST, National Astronomical Observatories, Chinese Academy of Sciences, Beijing 100101, China*

²*University of Chinese Academy of Sciences, Beijing 100049, China*

³*NAOC-UKZN Computational Astrophysics Centre, University of KwaZulu-Natal, Durban 4000, South Africa*

⁴*Chinese Academy of Sciences South America Center for Astronomy (CASSACA), NAOC, Beijing 100101, China*

⁵*Jet Propulsion Laboratory, California Institute of Technology, Pasadena, CA 91109, USA*

⁶*Jodrell Bank Centre for Astrophysics, Department of Physics and Astronomy, the University of Manchester, Oxford Road, Manchester, M13 9PL, UK*

ABSTRACT

We have analyzed the rotational properties of 12 clumps using ¹³CO (1–0) and C¹⁸O (1–0) maps of the Five College Radio Astronomy Observatory 13.7 m radio telescope. The clumps, located within molecular clouds, have radii (R) in the range of 0.06 – 0.27 pc. The direction of clump elongation is not correlated with the direction of the velocity gradient. We measured the specific angular momentum (J/M) to be between 0.0022 and 0.025 pc km s^{−1} based on ¹³CO images, and between 0.0025 and 0.021 pc km s^{−1} based on C¹⁸O images. The consistency of J/M based on different tracers indicates the ¹³CO and C¹⁸O in dense clumps trace essentially the same material despite significantly different opacities. We also found that J/M increases monotonically as a function of R in power-law form, $J/M \propto R^{1.58 \pm 0.11}$. The ratio between rotation energy and gravitational energy, β , ranges from 0.0012 to 0.018. The small values of β imply that rotation alone is not sufficient to support the clump against gravitational collapse.

Keywords: ISM:star formation — ISM: molecular cloud — ISM:kinematics and dynamics

1. INTRODUCTION

Molecular clouds are the major active star-forming regions in the Milk Way (Zuckerman & Palmer 1974; Burton 1976). Within are denser condensations (referred to as clumps) of size $\simeq 0.1$ pc, which are often gathered into larger-scale filamentary structures (see e.g. di Francesco et al. 2007). It is still arguable whether stars are born in a single system or in multiple systems (see e.g. Larson 2010). To understand the star-formation process, we really must trace the evolution of gas and dust starting at the scale of clouds, through clumps, down to the smaller scale of cores and finally to stars and stellar clusters. Molecular line emission plays a crucial role in the star formation process, as it is the primary coolant of gas at densities $\leq \simeq 10^6$ cm^{−3} when dust–gas coupling starts to dominate the thermal behavior (e.g.

Goldsmith 2001; Sipilä 2012). Wide-field maps of molecular lines offer rich kinematic information, based on the line profiles and their variation, but the main challenge for kinematic studies is the variation of molecular opacity, excitation, and abundance along the line of sight.

Thus, different molecular lines are chosen for different science goals. For example, the velocity gradient of N₂H⁺ (1–0) emission was used to investigate the angular momentum of cores in the Orion A cloud (Tatematsu et al. 2016). NH₃ inversion transitions (1,1) and (2,2) were used to derive the kinetic temperature of cores in the OMC2 and OMC3 regions of Orion (Li et al. 2013). A high angular and velocity resolution C¹⁸O (1–0) emission map was used to get an initial overview of the filamentary structure in the Orion A molecular cloud (Suri et al. 2019).

Rotation is one of the most fundamental physical parameters of cloud clumps. Besides affecting the mass distribution of the cloud clumps, rotation has the following important effects. First, it could provide additional support against collapse. For example, the rotation was left as a free parameter to fit emission spectra in Adams

Corresponding author: Xuefang Xu, Di Li, Y. Sophia Dai

xfxu@nao.cas.cn

dili@nao.cas.cn

yundai@nao.cas.cn

et al. (1987) models of young stellar objects (YSOs). Second, rotation can also twist magnetic-field lines by transferring the angular momentum from the cloud to the surrounding medium. This interaction between rotation and magnetic field was used to explain the angular momentum problem (e.g., Field 1978; Mouschovias & Paleologou 1979; Mouschovias 1987): the angular momentum of prestellar cores is many orders of magnitude larger than that can be contained within a single star, even though cores are observed to be rotating much less than originally predicted. Finally, when coupled with cloud morphology, the rotation rate affects possible fragmentation (i.e., formation of single or multiple prestellar objects) (e.g., Bodenheimer et al. 1980; Boss 1993; Xiao & Chang 2018).

β is the ratio between rotational energy and gravitational energy, which can be used to infer the dynamical status of cores, clumps and molecular clouds. In general, a large β (≥ 0.25 – 0.3) implies a stable gas cloud, which is not fragmenting and thus no longer forming stars. In a numerical simulation, Ostriker & Bodenheimer (1973) found that with $\beta = 0.25$ gravity is initially nearly balanced by rotation. On the other hand, a small β indicates instabilities against gravitational collapse. So far, this is the case for observed β values (see e.g. Goodman et al. 1993; Caselli et al. 2002; Chen et al. 2009; Li et al. 2012; Tatematsu et al. 2016). Several theoretical models have predicted specific β values to be associated with specific events, such as the formation of bars or rings ($\beta = 0.01$) (see e.g. Bodenheimer 1978; Rozyczka et al. 1980; Stahler 1983). Boss (1999) reported that rotating, magnetized cloud cores initially fragment when $\beta < 0.1$.

One way to measure the rotation is through large-scale velocity gradients. Large-scale velocity gradients are detected from molecular line emission maps. These gradients can be explained by rotation, outflow, infall, or motions between smaller unresolved clumps. Although it is difficult to distinguish definitively between these scenarios, the majority of previous researches have attributed observed velocity gradients to rotation (e.g. Clark & Johnson 1982; Kane & Clemens 1997; Pirogov et al. 2003; Redman et al. 2004; Shinnaga et al. 2004; Chen et al. 2007, 2009; Li et al. 2012). In our work, line wings were not detected and in consequence, outflows were not further considered. In general, velocity gradients can be obtained by linear fitting of velocity field ($v_{LSR} = v_0 + c_1\Delta\alpha + c_2\Delta\delta$) (Goodman et al. 1993), where the complex nature of the velocity field is ignored. It is assumed that clumps follow rigid-body rotation law and that the angular velocity is approximately the gradient of the line of sight velocity. This

is because turbulence is dominant in a larger scale than the size of clumps (e.g. Klapp et al. 2014). Thus rigid-body rotation is an appropriate approximation of the dense clumps.

Dominantly prograde velocity gradients are observed in the Colombo et al. (2014) cloud sample. Similar results were found by Braine et al. (2018) for M 33, and Braine et al. (2020) for M 51. The orientation of rotation axis in some studies has been found to be random (see e.g. Goodman et al. 1993; Caselli et al. 2002; Curtis & Richer 2011; Li et al. 2012; Tatematsu et al. 2016), or not, depending on the origin of the initial angular momentum of clouds. There are three or four orders of magnitude between the scale of the galaxies and that of dense clumps. Any robust relation was yet to be established between the rotation of dense clumps and the rotation of the Milky Way.

To measure the rotation, various tracers are utilized. Different molecular lines probes different excitation in different regions within the molecular clouds. In general, CO traces clouds. ^{13}CO and C^{18}O trace clumps. NH_3 and N_2H^+ trace cores. For instance, utilizing the $^{13}\text{CO}(1-0)$ map, Arquilla & Goldsmith (1986) found that molecular clouds B163 and B163SW rotate sufficiently relatively rapidly that the rotation is affecting their structure. Using $\text{C}^{18}\text{O}(3-2)$ map, Curtis & Richer (2011) studied clumps in the Perseus molecular cloud and found a dynamically insignificant rotation. Caselli et al. (2002) reached the same conclusion by mapping cores with $\text{N}_2\text{H}^+(1-0)$. Observationally, a universal power-law relation is found in dense cores/clumps between the specific angular momentum ($J/M = \text{angular momentum/core mass}$), and radius (R). J/M increases with R (i.e. $J/M \propto R^{1.6}$), for a typical $R \geq 0.02$ pc (Goodman et al. 1993). This relation can be used to indicate the initial conditions of the cores/clumps in a molecular cloud. The power-law relation is similar to Larson’s law (Larson 1981).

In this paper, we study the rotation in 12 clumps with the $^{13}\text{CO}(1-0)$ and $\text{C}^{18}\text{O}(1-0)$ maps. The clumps were identified using Two Micron All Sky Survey (2MASS) maps. The identified clumps are in 6 molecular clouds. This paper is organized as follows. Section 2 briefly describes data. Section 3 introduces the 6 molecular clouds in detail. In section 4, clump identification and velocity gradient fitting are introduced. We analyze the specific angular momentum in section 5. Section 6 is the discussion. We summarize the main results in section 7.

2. DATA

To study the clumps in molecular clouds, we observed 6 northern molecular clouds with the Five College Ra-

dio Astronomy Observatory (FCRAO) 13.7 m radio telescope. There are no protostars or YSOs in our clouds. The details of the clouds are given in section 3. The position and distance of the clouds were summarized in table 1. The $J=1 \rightarrow 0$ rotational transitions of ^{13}CO (110.201 GHz) and C^{18}O (109.782 GHz) were observed during 2001 May, 2003 April and May, and 2004 January.

The ^{13}CO and C^{18}O lines were observed simultaneously with the on-the-fly (OTF) mapping technique. The 15 pixel QUARRY (Quabbin Array Receiver) (Erickson et al. 1992) was employed to map L1523 and L1257. The autocorrelation spectrometer had a bandwidth of 20 MHz over 1024 channels, corresponding to a spectral resolution of 0.065 km/s at 110 GHz. The rest of the clouds were observed using the 32 pixel Sequoia receiver. The autocorrelation spectrometer had a bandwidth of 25 MHz over 1024 channels, corresponding to a spectral resolution of 0.067 km/s at 110 GHz. The angular size of the maps ranged from $15'$ to $34'$. The system temperature was typically 200 K and the integration time per beam on the sky was 10 s. The full width to half maximum beam widths were $45''$ and $48''$ for ^{13}CO and C^{18}O , respectively. To convert intensities from antenna temperature, T_A^* , to main beam temperature, T_{mb} , we used $T_{mb} = T_A^*/\eta_{mb}$ with $\eta_{mb} = 0.49$.

All observations used in this study were carried in a single program. The ^{13}CO and C^{18}O maps of L1523 and L1257 are published for the first time. For L1544, B227, L1574, and CB45, ^{13}CO and C^{18}O data were shown in Goldsmith & Li (2005). Zuo et al. (2018) used the ^{13}CO maps of B227, L1574, and CB45 to study H_2 formation.

The 2MASS extinction maps (Dobashi 2011) and ^{13}CO and C^{18}O maps have comparable angular resolution. The 2MASS maps were used to identify clumps as discussed in Section 4.1. Clump masses and sizes were calculated based on the results (the total intensity, semi-major and semi-minor axes of identified clumps) of the identification (see equations (1) and (2)).

3. SOURCES

3.1. L1544

L1544 is a well-observed molecular cloud associated with the Taurus dark cloud. There are no reported Infrared Astronomical Satellite (IRAS) sources associated with it (Beichman et al. 1986; Ward-Thompson et al. 1994; Doty et al. 2005). L1544 has a kinetic temperature of 9 K with a flat uniform radial flux density in inner region of radius 4800 AU (Kirk et al. 2005), an average density of $3 \times 10^6 \text{ cm}^{-3}$ within a radius of 500 AU (Keto & Caselli 2010), and extended inward

Table 1. Source list.

Sources	R.A. (J2000)	Dec. (J2000)	D	
			(pc)	References
L1544	05:04:18.10	+25:11:07.6	140	1
L1523	05:06:13.79	+31:43:59.8	140	2
B227	06:07:28.35	+19:28:03.8	400	3
L1574	06:08:04.95	+18:28:12.1	300	4
CB45	06:08:45.90	+17:53:15.2	300	4
L1257	23:57:31.87	+59:39:42.1	140	5

References for distance D. (1) Elias (1978); (2) Myers et al. (1983); (3) Bok & McCarthy (1974); (4) Kawamura et al. (1998); and (5) Snell (1981).

motions (Tafalla et al. 1998). Observations of water probing the densest central region together with those of carbon monoxide probing the more extended cloud have given almost unique information about the velocity field within this dense core. Only the unstable quasi-equilibrium Bonnor–Ebert (BE) sphere model was found to be consistent with molecular line observations of L1544 by Keto et al. (2015). The initial conditions of L1544 have been used as a testing ground for theories of low-mass star formation. For example, Whitworth & Ward-Thompson (2001) proposed an analytic model for the initial conditions of L1544. The model predicted the observed density profiles, the lifetimes, and the accretion rates of Class 0 protostars. The inferred infall velocities have been observed (Tafalla et al. 1998; Williams et al. 1999). For the distance of L1544, we use the average values (140 pc) from different techniques as described by Elias (1978).

3.2. L1523

L1523 is an isolated dark cloud without IRAS sources (Beichman et al. 1986) and has narrow ^{13}CO (1–0) line widths, indicating cold, quiet internal physical condition (Kim & Hong 2002; Kim et al. 2008). In addition, there is CO depletion in L1523. Myers et al. (1983) used ^{13}CO (1–0) and C^{18}O (1–0) to estimate a reliable distance of 140 pc for L1523.

3.3. B227

B227, also called L1570, is located in a complex region of considerable extinction with a Galactic latitude of $-0^\circ.46$. The cloud is approaching collapse (Stutz et al. 2009). The optical images of B227 show an opaque, elongated (along the North-South direction) core surrounded by a more diffuse dust structure. There is a prominent “ring” of H I self-absorption in B227, which implies that B227 is undergoing H_2 formation (Zuo et al. 2018). B227 is assumed to be at distances in the range between 400 pc and 600 pc (Hilton & Lahulla 1995) with

the most probable distance accepted for various studies being 400 pc (see e.g. Bok & McCarthy 1974; Goldsmith & Li 2005; Stutz et al. 2009; Zuo et al. 2018). For this work, we adopt the distance of 400 pc for B227.

3.4. L1574 and CB45

L1574 and CB45, also named L1578, were identified as isolated dark clouds, and coincidentally aligned in a linear configuration from north to south spanning about two degrees (Martin & Barrett 1978). Goldsmith & Li (2005) revealed that L1574 and CB45 have H I narrow self-absorption (HINSA) features using OH (Arecibo) and ^{13}CO and C^{18}O (FCRAO). There are no nearby UV sources such as massive stars or H II regions. Kawamura et al. (1998) lumped L1574 and CB45 together, and assigned them a distance of 300 pc.

3.5. L1257

L1257 is an elongated cloud from the southeast to the northwest, about 1° north of L1253. ^{13}CO and C^{18}O column densities of the cloud are power-law form, $\rho(r) \sim r^{-1}$ (Arquilla & Goldsmith 1985). Frerking & Langer (1982) found that the CO(1–0) line of L1257 has a possible pedestal feature and multiple components. Snell (1981) estimated a distance of 140 pc to L1257 by using V, (B–V) and MK spectral type of stars. He also determined the total mass of the cloud to be $35 M_\odot$ from ^{13}CO and H_2CO observations.

4. FITTING CLUMP AND VELOCITY GRADIENT

4.1. Identification of 2MASS Extinction Clumps with GAUSSCLUMPS

Clumps appear as enhancements of column density within clouds, and with reasonable generality we have assume an ellipsoid shape for the clumps. We used the GAUSSCLUMPS (Stutzki & Guesten 1990) code in the CUPID (Berry et al. 2007) package to identify clumps. This package is part of Starlink software¹. GAUSSCLUMPS searches for an ellipsoidal Gaussian density profile around the density peaks, and subtracts the fitted Gaussian ellipsoid from the data. It then iterates on the “clump removed data” until terminating criteria ($\text{MAXSKIP} \leq 50$, $\text{THRESH} \geq 5$, $\text{NPAD} \leq 50$, $\text{MINPIX} \geq 25$, $\text{MAXNF} \leq 200$) are reached (Table 2). Following the instructions of CUPID, we first subtracted the background with the FINDBACK procedure. After the background subtraction, we used the GAUSSCLUMPS to fit Gaussian components in the 2MASS extinction map. In the fitting process, “usable”

clumps are those that are well fitted with peak intensity five times higher than the Root Mean Square (rms) noise following Qian et al. (2012). A sample of 12 fitted clumps was thus obtained. Figure 1 shows the fitted clumps.

Table 2. Parameters used in the GAUSSCLUMPS method to identify clumps in the extinction map.

Parameter	Value
WWIDTH	2
WMIN	0.01
MAXSKIP	50
THRESH	5
NPAD	50
MAXBAD	0.05
VELORES	2
MODELLIM	0.05
MINPIX	25
FWHMBEAM	2
MAXCLUMPS	2147483647
MAXNF	200

Notes. **WWIDTH** is the ratio of the width of the weighting function, which is a Gaussian function, to that of the initial guessed Gaussian function.

WMIN: specifies the minimum weight. Pixels with weight less than this value are not included in the fitting process.

MAXSKIP: The iterative fitting process is terminated if more than “MAXSKIP” consecutive clumps cannot be fitted.

THRESH: gives the minimum peak amplitude of clumps to be fitted by GAUSSCLUMPS. The supplied value of “THRESH” is multiplied by the **rms** noise level before being used.

NPAD: The algorithm will terminate when “NPAD” consecutive clumps have been fitted with peak values less than the threshold value specified by the “THRESH” parameter (From the source code CUPID GaussClumps.c, one can see that the algorithm will do the same thing when “NPAD” consecutive clumps have pixels fewer than “MINPIX”).

MAXBAD: is the maximum fraction of bad pixels that may be included in a clump. Clumps will be excluded if they contain more bad pixels than this value.

VELORES: is the velocity resolution of the instrument in channels.

MODELLIM: is the model values that are treated as zero below ModelLim times the **rms** noise.

MINPIX: is the lowest number of pixel contained in a clump.

FWHMBEAM: is the FWHM of the instrument beam in pixels.

MAXCLUMPS: is an upper limit to the number of clumps to be fitted. It is set to be a very large number so that this parameter does not take effect.

MAXNF: is the maximum number of the allowed evaluations of the objective function when fitting an individual clump. Herein, it is just set to be a very large number to guarantee that all the clumps are fitted.

For fitted ellipsoids, the fitted clump radius can be defined as the geometrical mean of the semi-major (R_{major}) and semi-minor (R_{minor}) axes:

$$R = (R_{major}R_{minor})^{1/2}. \quad (1)$$

¹ <http://starlink.jach.hawaii.edu/starlink/>

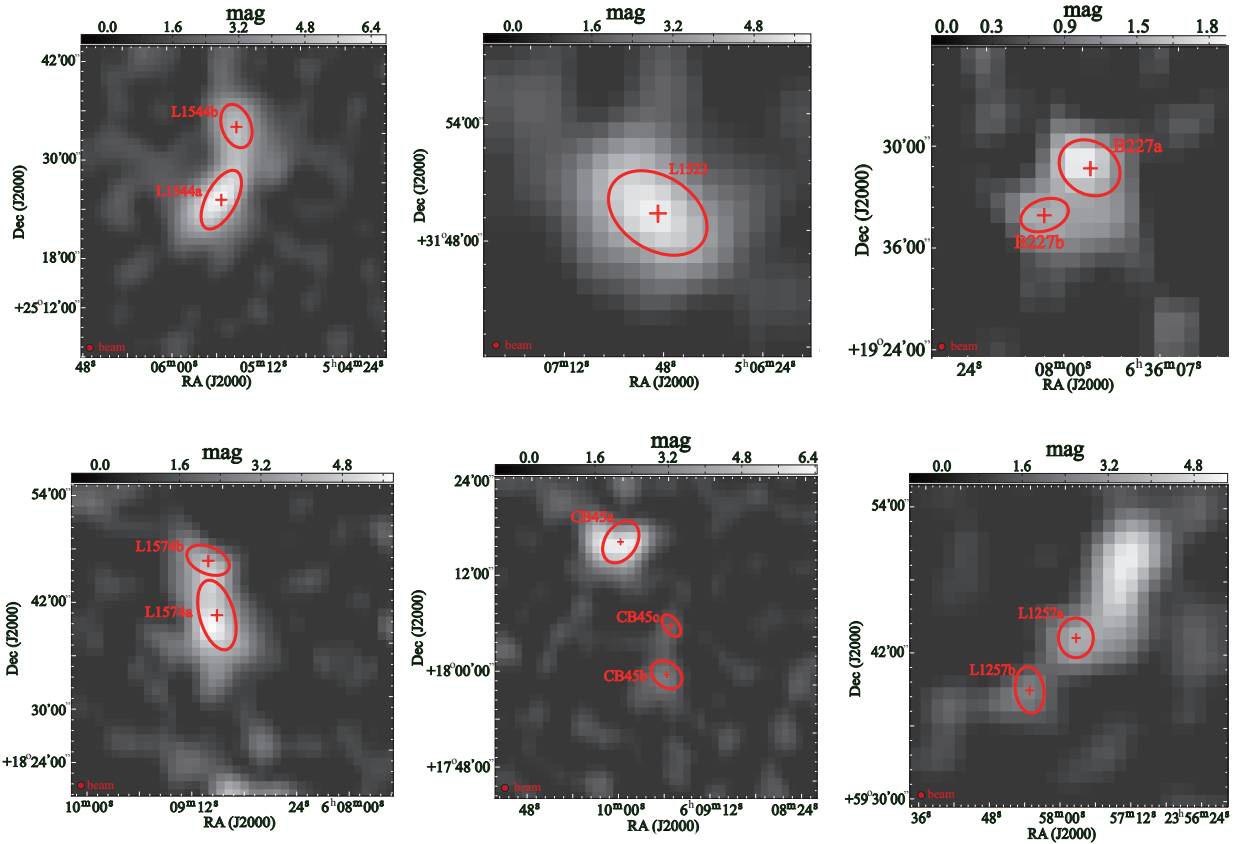


Figure 1. Clumps extracted from 2MASS extinction maps by utilizing GAUSSCLUMPS. The plus symbols denote the center position of each fitted clump. The coordinates of each plus symbol are listed in Table 3.

GAUSSCLUMPS outputs the total intensity, A_v^{tot} , which depends on the sum of all the pixels in each fitted clump. The fitted clump mass can be calculated by the following relation:

$$M = R^2 \mu \beta_v A_v^{tot}. \quad (2)$$

μ denotes the mean molecular weight corrected for the Helium (He) abundance. We take the Helium abundance to be $[H_e]/[H_2] = 2/9$ with $\mu = 2.88$. $\beta_v \simeq 1.9 \times 10^{21} \text{cm}^{-2} \text{mag}^{-1}$ is the ratio $(N(H_I) + 2N(H_2))/A_v$ (Bohlin et al. 1978). Table 3 gives the parameters of the fitted clumps.

The density profile is expected to have a power law form with a central core when the cloud is dominated by gravity (e.g. Ballesteros-Paredes et al. 2011; Chen et al. 2018). The Figure 1 of Keto & Caselli (2010) shows that density profiles of starless cores L1544 have an outer region where the density scales as $\rho \propto r^{-2}$ and an inner region ($\simeq 3.5''$) with constant density of $2 \times 10^7 \text{cm}^{-3}$. The sizes of our fitted L1544 clumps are much bigger than their inner regions. Figure 2 presents the $C^{18}O$ column density distribution in clump L1257a. We conclude that density increases from the outer region to the inner region in our fitted clumps. For the present work

we adopt a power-law profile density $\rho \propto r^{-1.6}$ (Bonnor 1956), which is reasonably close to various models (e.g. Keto & Caselli 2010; Li et al. 2013; Keto et al. 2015).

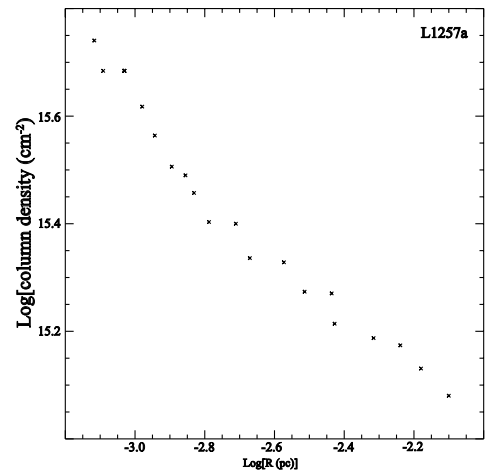


Figure 2. The distribution of the $C^{18}O$ column density in clump L1257a.

4.2. Line Fitting with CLASS

We used the CLASS software in GILDAS² to fit $^{13}\text{CO}(1-0)$ and $\text{C}^{18}\text{O}(1-0)$ spectral lines. Each spectrum was fit with a single Gaussian profile. There are three fit parameters in this process: the peak antenna temperature T_A^* , the line of sight velocity v_{LSR} , and the line width (full width at half-maximum, FWHM) Δv . The statistical uncertainties of each parameter were computed using expressions for the uncertainties obtained from Landman et al. (1982):

$$\sigma_{T_A^*} = 1.41 \left(\frac{\delta_v}{\Delta v} \right)^{1/2} \sigma_{rms}, \quad (3)$$

$$\sigma_{v_{LSR}} = 0.69 (\delta_v \Delta v)^{1/2} \frac{\sigma_{rms}}{T_A^*}. \quad (4)$$

δ_v is the velocity resolution and σ_{rms} is the rms noise in the spectrum.

We chose spectral lines to fit the velocity field of every fitted clump in three steps. First, we selected $^{13}\text{CO}(1-0)$ and $\text{C}^{18}\text{O}(1-0)$ spectral lines with peak intensity greater than three times of the rms noise and fitting errors. Figure 3 presents the two selected lines in the 6 molecular clouds. Second, these two lines in first step were located within the fitted 2MASS extinction image of the fitted clump. Third, the lines identified in the second step were then used to fit the velocity field. Table 4 presents the fitting results for all 12 identified clumps. The optical depth τ was calculated assuming that $^{13}\text{CO}(1-0)$ and C^{18}O are optically thick and thin, respectively, and that the temperature of the fitted clumps is 10 K.

4.3. Velocity Gradient Fitting

Rigid-body rotation in an molecular cloud produces a linear gradient, ∇v_{LSR} . In the local standard of rest (LSR) velocity field, the linear gradient is in a direction perpendicular to the rotation axis. We measured the velocity gradients following the method described in Goodman et al. (1993) fitting the function

$$v_{LSR} = v_0 + c_1 \Delta \alpha + c_2 \Delta \delta. \quad (5)$$

Here v_{LSR} represents an intensity weighted average velocity along the line of sight and v_0 is the systematic clump velocity, $\Delta \alpha$ and $\Delta \delta$ are the offsets from the center positions (see Table 1) of the ^{13}CO and C^{18}O images in the right ascension and declination in radians, respectively, and c_1 and c_2 are the projections of the gradient per radian onto the α and δ axes, respectively. The magnitude of the velocity gradient is defined by

$$\mathcal{G} = |\nabla v_{LSR}| = \frac{(c_1^2 + c_2^2)^{1/2}}{D}, \quad (6)$$

where D is the distance to the object. Its direction (i.e., the direction of the increasing velocity, measured east of north) is given by

$$\theta_{\mathcal{G}} = \tan^{-1} \frac{c_1}{c_2}. \quad (7)$$

We performed a least-squares fit to the Equation (5). Each value of v_{LSR} was weighted by $\sigma_{v_{LSR}}^{-2}$ (Equation (4)). The magnitude of the gradient (\mathcal{G}), its direction ($\theta_{\mathcal{G}}$), and their errors were calculated based on the results (c_1 and c_2) of the least-squares fit.

When a fitted clump has at least nine spatial pixels, its velocity gradient can be reliably fitted (Goodman et al. 1993). This applies to our 12 2MASS extinction clumps. All of the 12 clumps had well-fitted ^{13}CO , while 11 clumps, with the exception of B227b, had well-fitted C^{18}O lines. Beam smearing (inadequate spatial resolution) can possibly affect the fitting of velocity gradients. To test this, we have smoothed the spectral images of L1544 and B227, and then fitted the velocity gradient. We found that on average the finite beam size reduces the velocity gradient by 7.8%. Our sources are relatively near so that beam smearing should have only a minor impact on our results. For similar reasons, beam smearing was not discussed in the previous work on cloud rotation (Clark & Johnson 1982; Arquilla & Goldsmith 1986; Goodman et al. 1993; Kane & Clemens 1997; Caselli et al. 2002; Pirogov et al. 2003; Redman et al. 2004; Shinnaga et al. 2004; Chen et al. 2007, 2009; Li et al. 2012; Tatematsu et al. 2016).

The fitted \mathcal{G} and $\theta_{\mathcal{G}}$ are listed in Table 5 and plotted in Figure 4. The C^{18}O gradients are consistently larger than those of ^{13}CO . One possibility is that C^{18}O is better in tracing our fitted clumps. We also found that \mathcal{G} increases as M decreases, and that there is no obvious correlation between \mathcal{G} and R . Figure 5 shows the cumulative distribution function of $\theta_{\mathcal{G}}$, which is largely consistent with a random orientation.

5. SPECIFIC ANGULAR MOMENTUM ANALYSIS

5.1. Specific Angular Momentum

If molecular clouds are rotating, their present-day angular momentum could shed light on their evolution. The angular momentum per unit mass, j , is often used to compare the angular momenta at different regions with comparable mass. The specific angular momentum is given by

$$j = \frac{J}{M} = \frac{I\omega}{M} = p\omega R^2, \quad (8)$$

where $I = pMR^2$ denotes the moment of inertia for a fitted clump with power-law density distribution

² <http://www.iram.fr/IRAMFR/GILDAS>

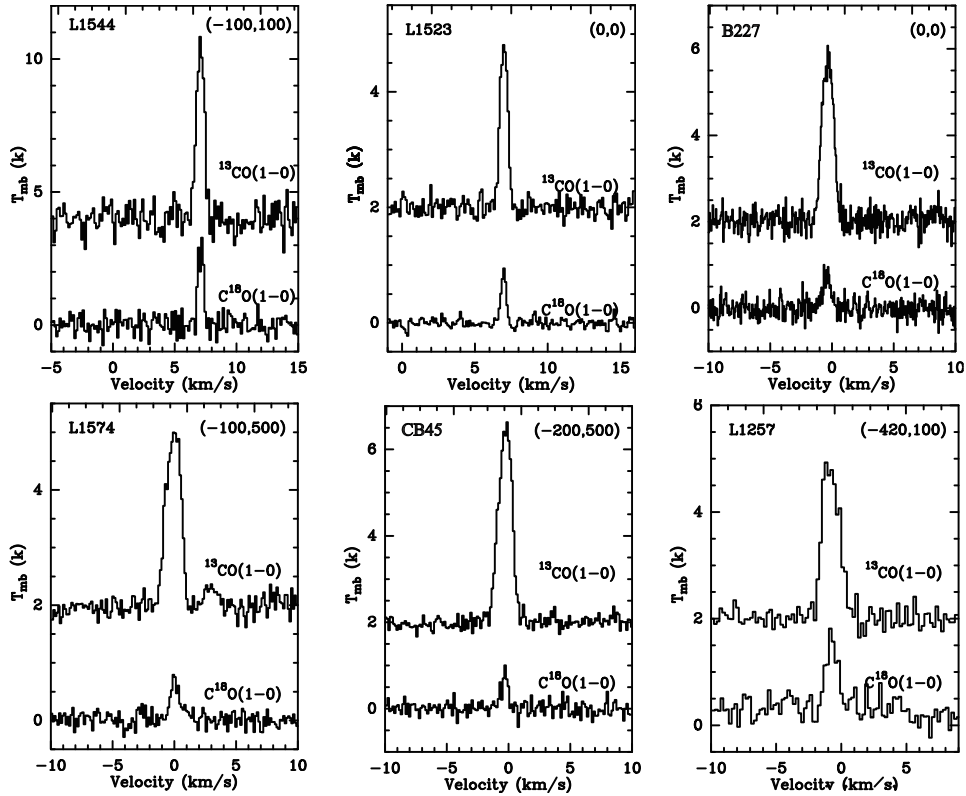


Figure 3. Spectra of ^{13}CO and C^{18}O in the six clouds included in this study. L1523 and B227 spectra are at the nominal central position of each cloud, while the offsets for L1544, L1574, CB45 and L1257 are in seconds of arc offset relative to the central position. The central positions are listed in Table 1.

($\rho \propto r^{-A}$). The correction factor (p) to the momentum of inertia due to density distribution can be expressed as

$$p = \frac{2(3 - A)}{3(5 - A)}. \quad (9)$$

The detailed derivation of p is shown in the Appendix A. $\omega = \mathcal{G}/\sin i$ is the angular velocity of the fitted clump, where i represents the inclination of ω to the line of sight. Assuming $\sin i = 1$, we find

$$J/M = \frac{2(3 - A)}{3(5 - A)} R^2. \quad (10)$$

The slope of the power-law density distribution was described in section 4.1. The assumption of $A = 1.6$ results in a 70% smaller specific angular momentum (J/M) than that of a uniform sphere. The calculated J/M of our fitted clumps is presented in Table 6 and plotted in Figure 6(a). The fitted power-law relation between J/M and R is $J/M \propto R^{1.58 \pm 0.11}$. Although marginally lower than what was found (1.6) in Goodman et al. (1993), our result generally agree with theirs.

Since we adopted $\sin i = 1$, but as we do not know the inclination of a given cloud along our line of sight, our determined ω could underestimate the true value

($\mathcal{G}/\sin i$). Therefore, our measurement of J/M is likely to be an underestimate, especially in a statistical sense.

5.2. Compare Rotational Energy with Gravitational Energy

In this section, we compare rotational energy with gravitational energy. Their ratio is defined as:

$$\beta = \frac{E_r}{E_g}, \quad (11)$$

where $E_r = \frac{1}{2}I\omega^2 = \frac{1}{2}pMR^2\omega^2$ denotes the rotational energy, and

$$E_g = -\frac{3}{5}\lambda\gamma\frac{GM^2}{R} \quad (12)$$

is the gravitational energy of the mass M within a radius R . The enhancement factor to the potential energy due to a power-law density profile is $\lambda = (1 - A/3)/(1 - 2A/5)$ (Li et al. 2013). γ represents the enhancement factor of gravitational potential due to deviation from spherical symmetry and can be calculated (Li et al. 2013) as

$$\gamma = \frac{\arcsin \sqrt{1 - f^2}}{\sqrt{1 - f^2}},$$

$$f = \frac{2}{\pi} f_{obs} \mathcal{F}_1(0.5, 0.5, -0.5, 1.5, 1, 1 - f_{obs}^2), \quad (13)$$

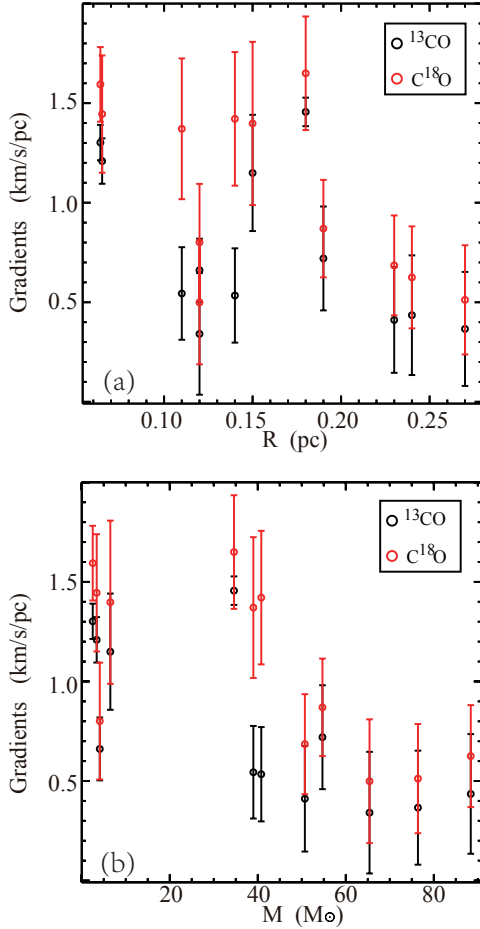


Figure 4. Velocity gradients correlated with (a) clump size, R and (b) clump mass, M .

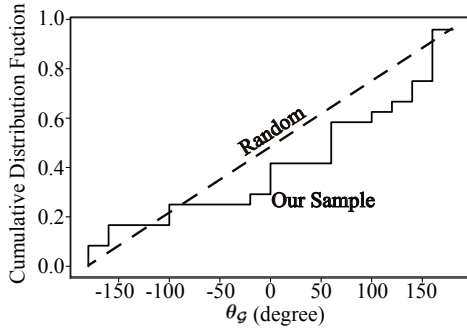


Figure 5. The cumulative distribution function of velocity gradient direction (θ_g).

where $f_{obs} = R_{minor}/R_{major}$ is the observed axis ratio of clumps, \mathcal{F}_1 denotes the Appell hypergeometric function in its first form. The γ value for each fitted clump is in Table 3.

The assumption of $\mathcal{A} = 1.6$ results in 70% smaller E_r and 31% bigger E_g , which add up to a factor of 2 lower β than that of a uniform sphere. For the inclination

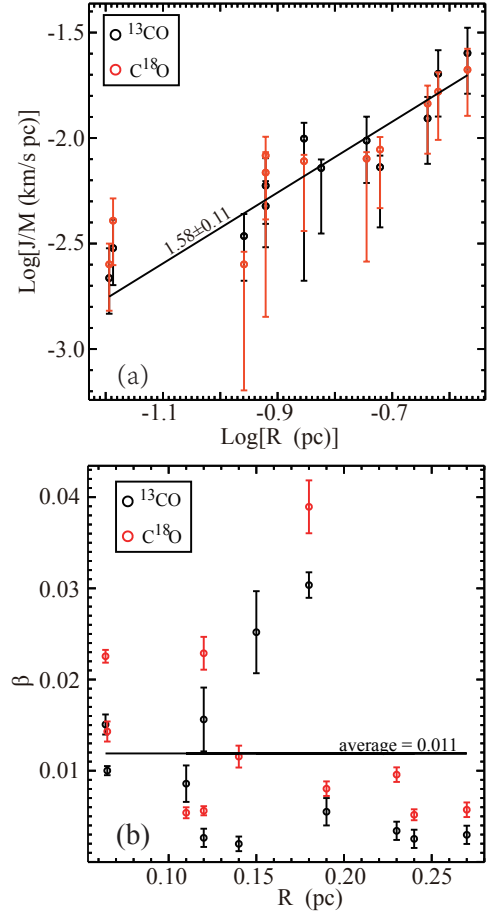


Figure 6. (a) J/M and (b) β correlated with clump size, R . The best power-law relation is obtained between J/M and R .

i , β is underestimated for the same reason as discussed above for J/M . The calculated β values can be found in Table 6 and were plotted in Figure 6(b). β does not vary with clump size R , and may be a constant independent of R . This conclusion is consistent with that of Goodman et al. (1993).

Rotational energy can be important for supporting dark cloud envelopes against gravitational collapse (e.g. Field 1978; Boss 1999; Dib et al. 2010). Rotation can prevent gravitational collapse when $\beta \geq 0.25$. It is difficult to determine the status of cores when $\beta < 0.1$. For our clumps, β ranges from 0.0012 to 0.018. These values are too small to prevent gravitational collapse of the clumps.

6. DISCUSSION

6.1. Comparison of ^{13}CO and C^{18}O Gradient Directions

Figure 7 shows the correlation between ^{13}CO and C^{18}O velocity gradient directions. We found a slope 1.05 ± 0.32 from the least squares linear fit, with a confi-

dence level of 75%. This significant correlation indicates that ^{13}CO and C^{18}O are tracing the same clump. Myers et al. (1991) proposed that there is a good correlation between position angles in different tracers for the same clump. This is confirmed by our results.

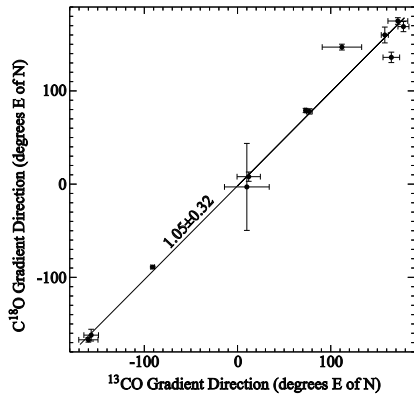


Figure 7. Comparison of gradient directions found using ^{13}CO and C^{18}O .

6.2. The Alignment Between Clump Elongation and Rotation Direction

Clump rotation sufficient to produce appreciable velocity gradients, can also lead to clumps being flattened along the axis of rotation. In our sample, the directions of velocity gradients are often different from the position angle of the long axis of a clump. The angular difference is likely random as shown in Figure 8. We note that there is no correlation between the clump elongation and the rotation direction. Figure 9 displays \mathcal{G} as a function of clump axial ratio, with no correlation being evident.

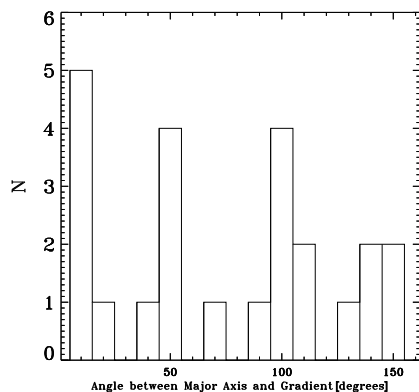


Figure 8. Distribution of angles between the major axis of each clump and the direction of its velocity gradient. Both ^{13}CO and C^{18}O gradient directions of each clump are included.

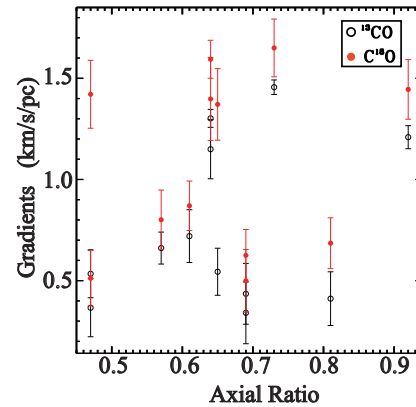


Figure 9. Velocity gradients correlation with the axial ratio of clumps.

6.3. J/M and β in This Study and Previous Studies

We compare the J/M and β values in our sample with those found in previous studies. Figure 10(a) compares J/M and β . There exists a power-law relation between J/M and clump size R for the entire ensemble of measurements, given by $J/M \propto R^{1.52 \pm 0.13}$. The value of the slope, 1.52, and its 1 sigma uncertainties, ± 0.13 , form a well-defined region (the shaded region of Figure 10(a)). The value 1.52 is consistent with value of 1.58, the best-fit value for the clumps studied here. β shows a large scatter, but the small value of β indicates that the rotational energy is a small fraction of the gravitational energy. Thus, the observed rotation alone cannot stop the gravitational collapse of the clumps found in molecular clouds.

Figure 10(c) plots the distribution of all clumps with J/M and R binned. The average values of J/M and β were calculated for each bin. We found that the binned J/M and β has similar trend as Figure 10(a) shown. The power-law relation between J/M and R applies over a range of spatial scales (0.006 – 42.0 pc). Due to the reduced scatter, we see that there is no evident relationship between β and R .

7. SUMMARY

We have mapped ^{13}CO and C^{18}O $J = 1-0$ emission from 6 molecular clouds. The rotation properties of the identified clumps were studied based on the velocity gradients. Our results are summarized as follows.

1. We used GAUSSCLUMPS to identify clumps with the 2MASS extinction images and identified 12 clumps in 6 molecular clouds. All clumps, except for B227b in C^{18}O , can be well fitted by single Gaussians, yielding velocity gradients between 0.34 and 1.46 $\text{km s}^{-1} \text{pc}^{-1}$ for ^{13}CO and between 0.50 and 1.65 $\text{km s}^{-1} \text{pc}^{-1}$ for C^{18}O .

2. The specific angular momentum (J/M) and the ratio between rotation energy and gravitational energy (β)

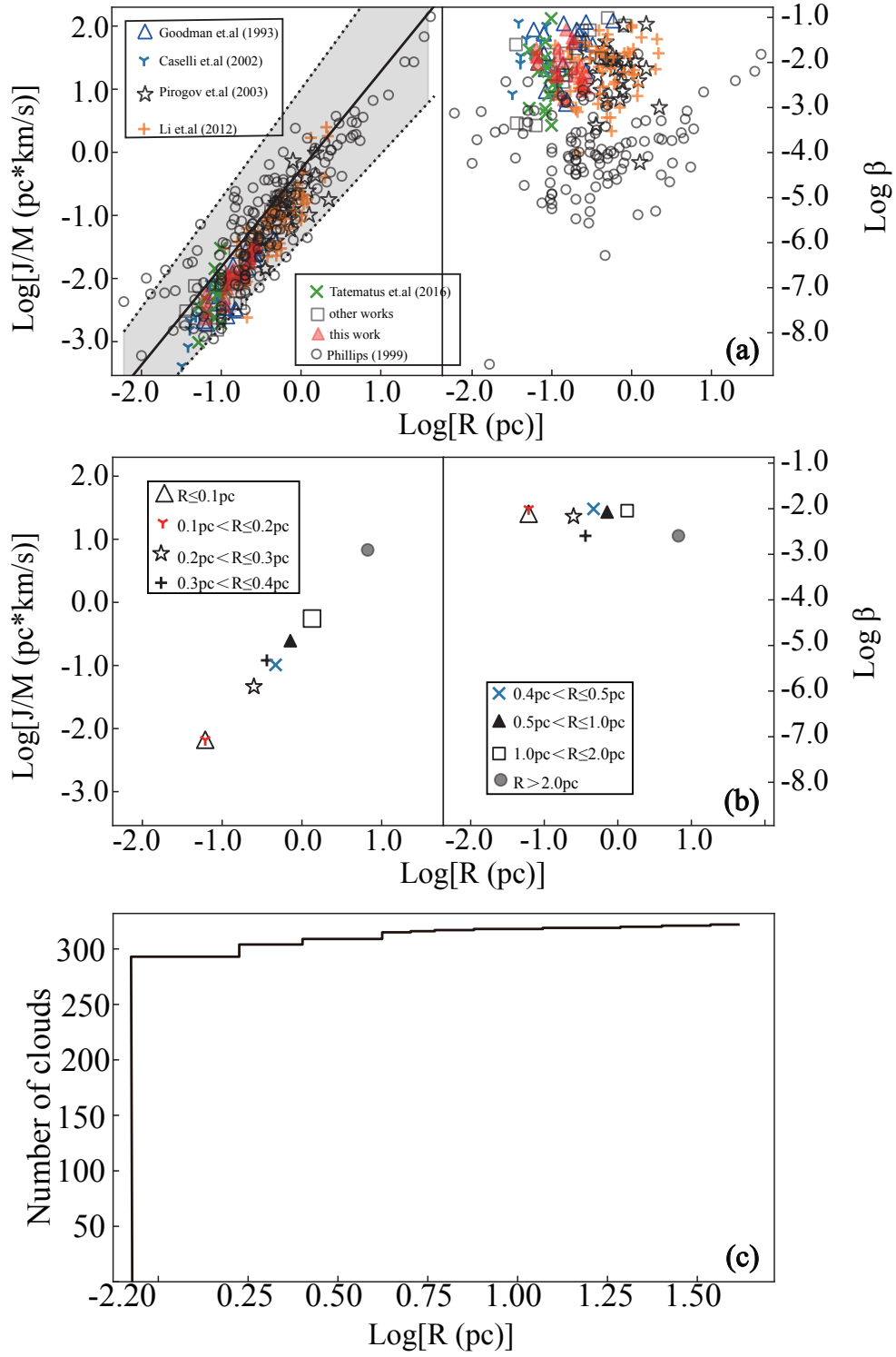


Figure 10. (a) Specific angular momentum (J/M) and the ratio of rotational to gravitational energy (β) as a function of R for the clumps in the present study together with those previously observed. The left panel shows the best-fit slope, 1.52, for $\log J/M$ vs $\log R$. The dotted lines denote the best-fit slope with ± 0.13 uncertainties. The right panel displays β vs R . (b) Averages J/M and β as a function of R . (c) Distribution of combined samples in this and previous studies as function of R .

were calculated from the measured velocity gradients. We adopted a more realistic assumption of a power-law density profile $\rho \propto r^{-1.6}$, resulting in 30% lower J/M and 50% lower β than those of the more commonly assumed spheres of uniform densities.

3. The calculated J/M ranges from 0.0022 to $0.025 \text{ pc km s}^{-1}$ for ^{13}CO , and from 0.0025 to $0.021 \text{ pc km s}^{-1}$ for C^{18}O . This indicates that J/M does not have significant evolution in the material traced by ^{13}CO compared to that traced by C^{18}O in dense clumps. There is a power-law relation between the J/M and the clump size (R), $J/M \propto R^{1.58 \pm 0.11}$, which is in general agreement with that found in [Goodman et al. \(1993\)](#).

4. The calculated β ranges from 0.0012 to 0.018 and is independent of R . The small value of β indicates that rotation alone cannot support the clumps against gravitational collapse.

5. The direction of clump elongation does not correlate with the direction of the velocity gradient.

6. We assembled the J/M and β measurements from literatures and studied their relation to R , along with

our results. For the combined data set, J/M also increases monotonically with R ($J/M \propto R^{1.52 \pm 0.13}$). The slope value of 1.52 is consistent with that of our sample alone (1.58).

7. The binned average J/M and β are well-correlated with R , and exhibit a similar trend as described above. We found that the power-law relation between J/M and R applies over a range of spatial scales of 0.006 to 42 pc.

We thank the referee for his constructive suggestions. This work is supported by the National Natural Science Foundation of China grant No. 11988101, No. 11725313, No. 11721303, the International Partnership Program of Chinese Academy of Sciences grant No. 114A11KYSB20160008, and the National Key R&D Program of China No. 2016YFA0400702. This work was carried out in part at the Jet Propulsion Laboratory, California Institute of Technology, under a contract with the National Aeronautics and Space Administration (80NM0018D0004).

APPENDIX

A. THE MOMENT OF INERTIA DERIVATION

The equation of a sphere (figure A1) with radius, r , is

$$x^2 + y^2 + z^2 = r^2. \quad (\text{A1})$$

Applying spherical coordinate transformation

$$\begin{cases} x = r \sin \theta \cos \varphi \\ y = r \sin \theta \sin \varphi \\ z = r \cos \theta \end{cases} \quad (\text{A2})$$

to the volume equation ($V = \frac{4}{3}\pi r^3$) of the sphere, we can obtain the differential volume element

$$dV = r^2 \sin \theta d\theta dr d\varphi. \quad (\text{A3})$$

$0 \leq \theta \leq \pi$ and $0 \leq \varphi \leq 2\pi$ are shown in figure. The density profile for the sphere is

$$\rho = r^{-A}. \quad (\text{A4})$$

Then the moment of inertia of the sphere about z axis can be calculated by

$$I = \int \int \int (x^2 + y^2) \rho dV = \int r^{4-A} dr \int_0^\pi \sin^3 \theta d\theta \int_0^{2\pi} d\varphi. \quad (\text{A5})$$

$$\int_0^\pi \sin^3 \theta d\theta = \frac{4}{3}, \quad (\text{A6})$$

and

$$\int_0^{2\pi} d\varphi = 2\pi \quad (\text{A7})$$

are easily gotten. Consequently,

$$I = \frac{8\pi}{3(5-\mathcal{A})} r^{5-\mathcal{A}} = \frac{2(3-\mathcal{A})}{3(5-\mathcal{A})} mr^2, \quad (\text{A8})$$

where

$$m = \int \rho dV = \int r^{2-\mathcal{A}} dr \int_0^\pi \sin \theta d\theta \int_0^{2\pi} d\varphi = \frac{4\pi}{3-\mathcal{A}} r^{3-\mathcal{A}}. \quad (\text{A9})$$

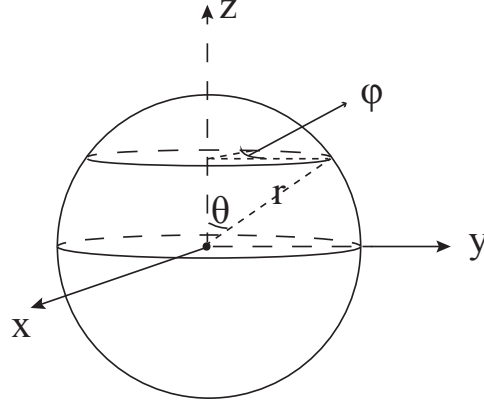


Figure A1. The point (0, 0, 0) located in the center of the sphere.

REFERENCES

- Adams, F. C., Lada, C. J., & Shu, F. H. 1987, *ApJ*, 312, 788
- Arquilla, R., & Goldsmith, P. F. 1985, *ApJ*, 297, 436
- Arquilla, R., & Goldsmith, P. F. 1986, *ApJ*, 303, 356
- Ballesteros-Paredes, J., Vázquez-Semadeni, E., Gazol, A., et al. 2011, *MNRAS*, 416, 1436
- Beichman, C. A., Myers, P. C., Emerson, J. P., et al. 1986, *ApJ*, 307, 337
- Berry, D. S., Reinhold, K., Jenness, T., et al. 2007, *Astronomical Data Analysis Software and Systems XVI*, 425
- Bodenheimer, P. 1978, *ApJ*, 224, 488
- Bodenheimer, P., Tohline, J. E., & Black, D. C. 1980, *ApJ*, 242, 209
- Bohlin, R. C., Savage, B. D., & Drake, J. F. 1978, *ApJ*, 224, 132
- Bok, B. J., & McCarthy, C. C. 1974, *AJ*, 79, 42
- Bonnor, W. B. 1956, *MNRAS*, 116, 351
- Boss, A. P. 1993, *ApJ*, 410, 157
- Boss, A. P. 1999, *ApJ*, 520, 744
- Braine, J., Rosolowsky, E., Gratier, P., et al. 2018, *A&A*, 612, A51
- Braine, J., Hughes, A., Rosolowsky, E., et al. 2020, *A&A*, 633, A17
- Burton, W. B. 1976, *ARA&A*, 14, 275
- Caselli, P., Benson, P. J., Myers, P. C., et al. 2002, *ApJ*, 572, 238
- Chen, X., Launhardt, R., & Henning, T. 2007, *ApJ*, 669, 1058
- Chen, X., Launhardt, R., & Henning, T. 2009, *ApJ*, 691, 1729
- Chen, H. H.-H., Burkhardt, B., Goodman, A., et al. 2018, *ApJ*, 859, 162
- Clark, F. O., & Johnson, D. R. 1982, *ApJ*, 263, 160
- Colombo, D., Hughes, A., Schinnerer, E., et al. 2014, *ApJ*, 784, 3
- Curtis, E. I., & Richer, J. S. 2011, *MNRAS*, 410, 75
- Dib, S., Hennebelle, P., Pineda, J. E., et al. 2010, *ApJ*, 723, 425
- Dobashi, K. 2011, *PASJ*, 63, S1
- Doty, S. D., Everett, S. E., Shirley, Y. L., et al. 2005, *MNRAS*, 359, 228
- Elias, J. H. 1978, *ApJ*, 224, 857
- Erickson, N. R., Goldsmith, P. F., Novak, G., et al. 1992, *IEEE Transactions on Microwave Theory Techniques*, 40, 1
- Field, G. B. 1978, *IAU Colloq. 52: Protostars and Planets*, 243
- di Francesco, J., Evans, N. J., Caselli, P., et al. 2007, *Protostars and Planets V*, 17

- Frerking, M. A., & Langer, W. D. 1982, *ApJ*, 256, 523
- Goldsmith, P. F. 2001, *ApJ*, 557, 736
- Goldsmith, P. F., & Li, D. 2005, *ApJ*, 622, 938
- Goodman, A. A., Benson, P. J., Fuller, G. A., et al. 1993, *ApJ*, 406, 528
- Hilton, J., & Lahulla, J. F. 1995, *A&AS*, 113, 325
- Kane, B. D., & Clemens, D. P. 1997, *AJ*, 113, 1799
- Kawamura, A., Onishi, T., Yonekura, Y., et al. 1998, *ApJS*, 117, 387
- Keto, E., & Caselli, P. 2010, *MNRAS*, 402, 1625
- Keto, E., Caselli, P., & Rawlings, J. 2015, *MNRAS*, 446, 3731
- Kim, H. G., & Hong, S. S. 2002, *ApJ*, 567, 376
- Kim, H. G., Kim, B. G., & Jung, J. H. 2008, *ChJA&A*, 8, 686
- Kirk, J. M., Ward-Thompson, D., & André, P. 2005, *MNRAS*, 360, 1506
- Klapp, J., Sigalotti, L. D. G., Zavala, M., et al. 2014, *ApJ*, 780, 188
- Landman, D. A., Roussel-Dupre, R., & Tanigawa, G. 1982, *ApJ*, 261, 732
- Larson, R. B. 1981, *MNRAS*, 194, 809
- Larson, R. B. 2010, *Reports on Progress in Physics*, 73, 014901
- Li, D., Kauffmann, J., Zhang, Q., et al. 2013, *ApJL*, 768, L5
- Li, J., Wang, J., Gu, Q., et al. 2012, *ApJ*, 745, 47
- Martin, R. N., & Barrett, A. H. 1978, *ApJS*, 36, 1
- Mouschovias, T. C., & Paleologou, E. V. 1979, *ApJ*, 230, 204
- Mouschovias, T. C. 1987, *NATO ASIC Proc. 210: Physical Processes in Interstellar Clouds*, 453
- Myers, P. C., Linke, R. A., & Benson, P. J. 1983, *ApJ*, 264, 517
- Myers, P. C., Fuller, G. A., Goodman, A. A., et al. 1991, *ApJ*, 376, 561
- Ostriker, J. P., & Bodenheimer, P. 1973, *ApJ*, 180, 171
- Pirogov, L., Zinchenko, I., Caselli, P., et al. 2003, *A&A*, 405, 639
- Qian, L., Li, D., & Goldsmith, P. F. 2012, *ApJ*, 760, 147
- Redman, M. P., Keto, E., Rawlings, J. M. C., et al. 2004, *MNRAS*, 352, 1365
- Rozyczka, M., Tscharnuter, W. M., & Yorke, H. W. 1980, *A&A*, 81, 347
- Shinnaga, H., Ohashi, N., Lee, S.-W., et al. 2004, *ApJ*, 601, 962
- Sipilä, O. 2012, *A&A*, 543, A38
- Snell, R. L. 1981, *ApJS*, 45, 121
- Stahler, S. W. 1983, *ApJ*, 268, 165
- Stutz, A. M., Rieke, G. H., Bieging, J. H., et al. 2009, *ApJ*, 707, 137
- Stutzki, J., & Guesten, R. 1990, *ApJ*, 356, 513
- Suri, S., Sánchez-Monge, Á., Schilke, P., et al. 2019, *A&A*, 623, A142
- Tafalla, M., Mardones, D., Myers, P. C., et al. 1998, *ApJ*, 504, 900
- Tatematsu, K., Ohashi, S., Sanhueza, P., et al. 2016, *PASJ*, 68, 24
- Ward-Thompson, D., Scott, P. F., Hills, R. E., et al. 1994, *MNRAS*, 268, 276
- Whitworth, A. P., & Ward-Thompson, D. 2001, *ApJ*, 547, 317
- Williams, J. P., Myers, P. C., Wilner, D. J., et al. 1999, *ApJL*, 513, L61
- Xiao, L., & Chang, Q. 2018, *ApJ*, 853, 22
- Zuckerman, B., & Palmer, P. 1974, *ARA&A*, 12, 279
- Zuo, P., Li, D., Peek, J. E. G., et al. 2018, *ApJ*, 867, 13

Table 3. Properties of the fitted clumps observed in 2MASS extinction map.

clumps	R.A. , Decl. (J20000) (h:m:s, °:':")	M (M_{\odot})	R (pc)	R_{major} (pc)	R_{minor} (pc)	Angle (deg E of N)	f_{obs}	γ
L1544a	05:04:24.21,+25:13:53.1	40.8	0.14	0.20	0.09	-17	0.47	1.29
L1544b	05:03:46.96,+25:21:29.4	39.0	0.11	0.14	0.09	65	0.65	1.19
L1523	05:06:16.32,+31:43:58.6	65.4	0.12	0.14	0.10	-102	0.69	1.17
B227a	06:07:27.06,+19:29:33.2	50.7	0.23	0.25	0.21	-57	0.81	1.10
B227b	06:07:44.89,+19:28:14.7	6.5	0.15	0.19	0.12	109	0.64	1.20
L1574a	06:08:13.02,+18:31:49.0	76.4	0.27	0.40	0.19	-110	0.47	1.30
L1574b	06:08:02.69,+18:38:29.9	54.7	0.19	0.25	0.15	-120	0.61	1.21
CB45a	06:08:44.25,+18:07:29.1	88.4	0.24	0.29	0.20	147	0.69	1.17
CB45b	06:08:58.87,+17:47:43.2	34.6	0.18	0.21	0.15	55	0.73	1.14
CB45c	06:08:42.05,+17:53:31.7	4.1	0.12	0.16	0.09	37	0.57	1.23
L1257a	23:57:26.04,+59:40:14.7	3.4	0.07	0.07	0.06	-2	0.92	1.04
L1257b	23:58:04.72,+59:36:48.5	2.5	0.06	0.08	0.05	-9	0.64	1.19

Notes. Columns are (1) identified clumps, (2) coordinates of clumps center position, (3) mass of clumps, (4) clump radius, (5) clump semi-major axis, (6) clump semi-minor axis, (7) clump orientations, (8) clump axis ratio, (9) enhancement factor (see Equation (13) in Section 5.2 and Li et al. (2013)).

Table 4. Results of spectral line fitting.

clumps	^{13}CO				C^{18}O			
	T_A^* K	V_{LSR} (km/s)	ΔV_{FWHM} (km/s)	τ	T_A^* K	V_{LSR} (km/s)	ΔV_{FWHM} (km/s)	τ
L1544a	1.34 ± 0.07	-0.87 ± 0.02	0.83 ± 0.04	0.32	0.16 ± 0.01	-0.35 ± 0.03	0.70 ± 0.08	0.03
L1544b	1.73 ± 0.05	-0.93 ± 0.01	0.87 ± 0.03	0.44	0.13 ± 0.01	-0.31 ± 0.04	0.77 ± 0.09	0.03
L1523	2.40 ± 0.03	-0.44 ± 0.01	1.48 ± 0.01	0.67	0.23 ± 0.02	-0.48 ± 0.02	0.63 ± 0.04	0.05
B227a	2.42 ± 0.02	0.72 ± 0.01	1.33 ± 0.01	0.68	0.24 ± 0.02	-0.25 ± 0.01	0.72 ± 0.03	0.05
B227b	1.59 ± 0.02	0.35 ± 0.01	1.58 ± 0.01	0.39	0.46 ± 0.02	-0.55 ± 0.01	0.83 ± 0.03	0.09
L1574a	3.30 ± 0.04	-0.43 ± 0.01	1.09 ± 0.01	1.12	0.35 ± 0.01	-0.51 ± 0.01	0.59 ± 0.02	0.07
L1574b	2.61 ± 0.24	-0.31 ± 0.03	0.86 ± 0.04	0.76	0.09 ± 0.01	-0.60 ± 0.07	0.90 ± 0.19	0.02
CB45a	3.84 ± 0.09	7.02 ± 0.01	0.53 ± 0.02	1.54	0.56 ± 0.02	7.01 ± 0.01	0.30 ± 0.01	0.11
CB45b	3.93 ± 0.03	7.04 ± 0.01	0.67 ± 0.01	1.62	0.45 ± 0.02	6.92 ± 0.01	0.37 ± 0.01	0.09
CB45c	3.64 ± 0.03	7.14 ± 0.01	0.66 ± 0.01	1.36	0.46 ± 0.02	7.11 ± 0.01	0.45 ± 0.01	0.09
L1257a	2.74 ± 0.01	-0.69 ± 0.01	1.47 ± 0.01	0.82	0.44 ± 0.01	-0.77 ± 0.01	1.12 ± 0.02	0.09
L1257b	1.98 ± 0.03	-0.30 ± 0.01	1.30 ± 0.02	0.52	0.27 ± 0.02	-0.44 ± 0.04	1.23 ± 0.08	0.06

Table 5. Results of velocity gradient fitting.

clumps	^{13}CO			C^{18}O		
	N	\mathcal{G} (km/s/pc)	$\theta_{\mathcal{G}}$ (deg E of N)	N	\mathcal{G} (km/s/pc)	$\theta_{\mathcal{G}}$ (deg E of N)
L1544a	360	0.53 ± 0.13	73 ± 2	84	1.42 ± 0.47	79 ± 9
L1544b	364	0.54 ± 0.13	77 ± 8	408	1.37 ± 0.48	78 ± 11
L1523	63	0.34 ± 0.10	91 ± 6	58	0.50 ± 0.16	-89 ± 4
B227a	176	0.41 ± 0.11	10 ± 8	49	0.69 ± 0.17	-3 ± 7
B227b	126	1.15 ± 0.34	12 ± 5	6	—	—
L1574a	498	0.37 ± 0.11	-157 ± 41	147	0.51 ± 0.14	-162 ± 51
L1574b	390	0.72 ± 0.19	-160 ± 55	57	0.87 ± 0.21	-167 ± 21
CB45a	1216	0.44 ± 0.14	165 ± 49	85	0.63 ± 0.16	136 ± 38
CB45b	316	1.46 ± 0.11	158 ± 20	84	1.65 ± 0.47	160 ± 68
CB45c	520	0.66 ± 0.10	172 ± 61	132	0.80 ± 0.24	175 ± 31
L1257a	143	1.21 ± 0.12	112 ± 79	74	1.45 ± 0.43	147 ± 23
L1257b	142	1.31 ± 0.12	178 ± 35	36	1.59 ± 0.30	169 ± 46

Notes. — Clump B227b has fewer than nine chosen C^{18}O spectral lines and in consequence could not be reliably fitted. **N is the number of the chosen ^{13}CO and C^{18}O spectral lines.**

Table 6. Calculated J/M and β based on the fitted velocity gradients.

clumps	^{13}CO		C^{18}O	
	J/M (pc km/s)	β	J/M (pc km/s)	β
L1544a	0.0099 ± 0.0003	0.0012 ± 0.0008	0.0078 ± 0.0004	0.0086 ± 0.001
L1544b	0.0034 ± 0.0004	0.0039 ± 0.0004	0.0025 ± 0.0002	0.0025 ± 0.0006
L1523	0.0060 ± 0.0004	0.0014 ± 0.0002	0.0083 ± 0.0006	0.0026 ± 0.0005
B227a	0.012 ± 0.0002	0.0016 ± 0.0002	0.015 ± 0.0003	0.0044 ± 0.0004
B227b	0.0072 ± 0.002	0.011 ± 0.005	—	—
L1574a	0.025 ± 0.002	0.0014 ± 0.0002	0.021 ± 0.003	0.0026 ± 0.0004
L1574b	0.0073 ± 0.002	0.0025 ± 0.0003	0.0088 ± 0.0003	0.0037 ± 0.0004
CB45a	0.020 ± 0.002	0.0012 ± 0.0002	0.017 ± 0.003	0.0024 ± 0.0003
CB45b	0.0097 ± 0.001	0.014 ± 0.001	0.0080 ± 0.0004	0.018 ± 0.003
CB45c	0.0047 ± 0.0004	0.0071 ± 0.004	0.0069 ± 0.001	0.010 ± 0.002
L1257a	0.0030 ± 0.0001	0.0046 ± 0.0001	0.0041 ± 0.0005	0.0065 ± 0.001
L1257b	0.0022 ± 0.0001	0.069 ± 0.001	0.0025 ± 0.0004	0.010 ± 0.0007